AIAA JOURNAL
Vol. 48, No. 6, June 2010

Investigation of the Taylor–Culick Flow Through Particle Image Velocimetry and Numerical Simulation

D. Laboureur,* B. Tóth,† and J. Anthoine‡
von Karman Institute for Fluid Dynamics, 1640 Rhode-St-Genèse, Belgium

DOI: 10.2514/1.44616

The Taylor–Culick flow corresponds to the flow injection through the lateral wall of a semi-infinite channel. This flow is intrinsically unstable downstream of a critical axial position. The flow disturbances develop in vortices that could couple with the acoustics of the channel, generating pressure oscillations. This is what occurs in large solid rocket motors in which the Taylor flow is induced by the propellant combustion. Depending mainly on the Reynolds number, three different flow regimes can be observed: laminar, transitional, or turbulent. The current paper presents an experimental and numerical investigation of that flow instability. The setup consists of a rectangular shape channel in which air is introduced through the bottom wall due to a porous plate. Quantitative measurements are performed with particle image velocimetry while unsteady numerical simulations are carried out using large eddy simulation. A special injection system for the seeding particles and a special arrangement for the laser sheet provide good quality particle image velocimetry data. The numerical simulations are validated against the particle image velocimetry results. They complete the particle image velocimetry investigation by following chronologically the instantaneous phenomenon. The experiments and the numerical simulations are performed at different injection velocities and channel heights.

Nomenclature

D	=	diameter of detected vortices
f_{cut}	=	cutoff frequency
f_s	=	cutoff frequency
h	=	channel height
L	=	total length
V_{inj}	=	injection velocity
x	=	axial coordinate
x_D	=	axial position where coherent structures are produced
x_S	=	nondimensional outlet abscissa
x_T	=	axial position where the flow becomes turbulent
y	=	transversal coordinate
λ	=	lambda field

Introduction

LARGE solid rocket motors (SRMs) are composed of a submerged nozzle and segmented propellant grains separated by inhibitors. When ignited, the propellant of the Ariane 5 solid rocket motor starts to burn on its internal surface, consuming the grain radially. Hot burnt gas then originates, first radially from the burning surface of the combustion chamber, and then develops longitudinally before reaching the nozzle. This kind of flow is called Taylor–Culick flow [1,2].

During a few seconds of the shot, pressure oscillations are observed inside the booster and are due to aeroacoustic coupling [3–7]: the acoustic properties of the combustion chamber are excited by hydrodynamic instabilities. Similar results were also observed on subscaled model rockets [8,9] and from numerical simulations [10–13]. Cold gas experimental setups are developed in order to analyze primarily potential unstable mechanisms in the internal flowfield of the SRM. The reason for operating these facilities with cold gases remains in their low operating cost, and because combustion is believed to take a minor part in the instability mechanism. Cold flow experiments in a pipe with one or two inhibitors were conducted, for example, by Culick and Magiawala [14], Dunlap and Brown [15], Mettenleiter et al. [16], and Anthoine et al. [17]. Other cold gas facilities have been developed within the Aerodynamics of Segmented Solid Motors program focusing mainly on the hydrodynamic instability appearing in the Ariane 5 MPS [18]. Some of these facilities have been used more recently by Vetel et al. [19] to investigate the influence of the inhibitor shape, and by Nguyen et al. [20] to analyze the effect of the injecting wall inclination. Anthoine and Lema [21] have also performed cold gas experiments to determine the performance of passive control systems to reduce the pressure oscillations.

Numerical simulations are also used to highlight the hydrodynamic instabilities and their coupling with the acoustics [22–25]. More recently, the large eddy simulation (LES) approach has been applied to simulate the unsteady flow evolution in porous chambers by Apte and Yang [26–28], Vetel et al. [29] and Plourde et al. [30].

The previous studies showed that the hydrodynamic instabilities are organized in coherent structures. These structures can be formed by separated flow at the end of a propellant grain, acting as a backward facing step [31], or at the inhibitor, acting as an obstacle [32]. The instabilities can also come from the natural instability of the flow itself, especially the curvature of the streamlines [33]. This kind of instability is called surface vortex shedding (SVS). Flandro and Majdalani [34] use this concept of SVS to explain the instabilities in existing SRMs that do not have inhibitors. Chedevergne et al. [35] develop a stability analysis of the flow induced by wall injection. This paper is focusing on the investigation of such SVS instability.

Because the primary goal of the above cited cold gas setups is to analyze the unstable mechanism of flow-acoustic coupling, the resulting experimental database consists of unsteady pressure, mainly at the forward end, and a few velocity fluctuation profiles. The latter are obtained using either hot wire anemometry or laser doppler velocimetry. To characterize the unsteady internal flowfield of the complete facility and to generate a detailed database for the validation of the numerical simulations, the most promising technique is particle image velocimetry (PIV). PIV is a nonintrusive

Presented as Paper 5052 at the 44th AIAA/ASME/SAE/ASEE Joint Propulsion Conference and Exhibit, Hartford, USA, 21–23 July 2008; received 28 March 2009; revision received 6 January 2010; accepted for publication 2 February 2010.

*Ph.D. Candidate, Chaussée de Waterloo 72.

†Research Engineer. Present address: European Space Agency, Noordwijk, The Netherlands. Student Member AIAA.

‡Associate Professor. Present address: ONERA, Propulsion Laboratory, Midi-Pyrenees Center, Mauzac, France; jerome.anthoine@onera.fr. Member AIAA.

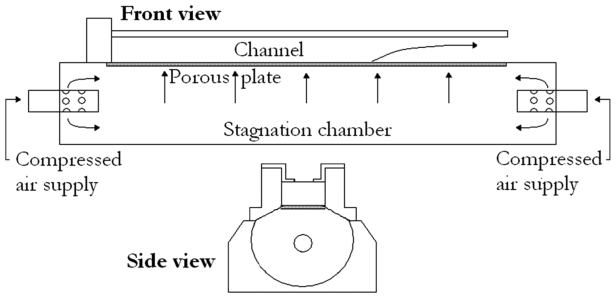

Fig. 1 Experimental setup.

measurement technique that provides instantaneous velocity vector fields [36]. This technique has not been applied to the cold gas facilities up to now except by Anthoine et al. [37], who used it only for the assessment of an adaptive control system and not for generating a database for numerical validation.

The spatial instabilities can be studied using an axisymmetric or a planar flow configuration. For the axisymmetric case a cylindrical channel is used, injecting air all over the surface through a porous media. For the planar case, a rectangular channel is used, injecting air through porous media along only one side.

For experimental purposes, axisymmetric subscale cold flow models exist at the von Karman Institute (VKI) and ONERA. The VKI model [38] consists of a porous cylindrical channel placed inside a stagnation chamber, which supplies air. It is mainly used for the investigation of the effect of the aft-end volume on the pressure oscillations. The ONERA model, called Valdo [39], also consists of a porous cylinder, but is supplied by compressed air through several prechambers. Both setups proved the presence of SVS. However, there is no visual access to the flow inside an axisymetric channel.

For the planar case, only two models were investigated at ONERA (Vecla [40]) and ENSMA (Micat1 [41]). Micat1 was built to investigate the three different types of instabilities, while Vecla was only dedicated to SVS. These setups proved the presence of instabilities by the analysis of velocity spectra coming from hot-wire measurements. In addition, a visualization of the vortex shedding was made using the planar laser-induced fluorescence technique in Vecla. These measurement campaigns showed that, by changing the injection velocity and the channel height, different types of flow regimes can be observed: laminar (in the whole channel), transitional (laminar in the upstream part of the channel and turbulent in the downstream part), and turbulent (in the whole channel).

Even if the previous works were able to prove the presence of SVS and to characterize the flow through velocity spectra, no whole-field measurements are available nowadays in the literature. Therefore, the objectives of this study are first to adapt the PIV technique to measure velocities in a channel, where the flow is injected through a porous plate, and to investigate the different flow regimes presented above. Numerical simulations are also performed to support the previous investigation by following chronologically the instantaneous phenomenon. All the configurations tested experimentally and computed numerically are listed in Table 1. The first configuration is chosen to be the nominal one.

Experimental Apparatus and Technique

The experimental apparatus is composed of a rectangular channel (Fig. 1). The lateral-, upper-, and head-end walls are closed, the rear-end is free. The channel is 0.6 m long, 0.06 m wide, and with a height that can be modified to be either 0.023 or 0.033 m. The flow in the channel is generated by the injection of compressed air at ambient temperature through a porous plate of 5 mm thickness made of Poral sintered-bronze spheres with a porosity of 100 μm. In this one-fortieth scale model of Ariane 5 P230 the most important non-dimensional number to respect for similitude is the Mach number, because the Reynolds number in the real booster is so high that the viscous effects are negligible. For the measurement campaign, the objective is to characterize the flow in the channel, trying to catch the three different types of flow. However, due to technical reasons, it was not possible experimentally to reach the conditions needed for the turbulent flow. The parameters of the measured configurations are listed in Table 1.

Table 1 Configurations of the channel investigated in this study

	h	V_{inj}	Type of flow	Approach
1	23 mm	1.5 m/s	Transitional	PIV and CFD
2	23 mm	1.0 m/s	Transitional	PIV
3	33 mm	1.0 m/s	Laminar	PIV and CFD
4	33 mm	1.5 m/s	Laminar	PIV
5	13 mm	2.0 m/s	Turbulent	CFD

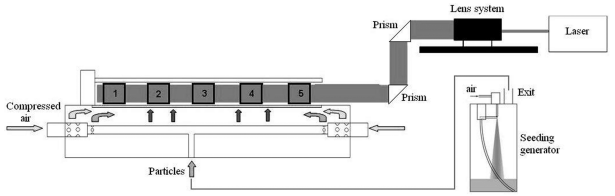

Fig. 2 Schematic view of the injection and laser sheet generation system.

The objective of this study is to obtain qualitative and quantitative information of the flow inside the experimental setup. Therefore, the PIV technique is used (Fig. 2). This technique requires the injection of oil seeding particles into the channel and the generation of a planar laser sheet. A special seeding generator was designed to inject particles inside the stagnation chamber through a T-tube whose extremities are placed close to the air injection to give the best air particles mixing and a uniform concentration in the channel. A collimated laser sheet (of constant height) was generated by a lens system, using a double pulsed Nd-Yag laser. The laser sheet illuminates the flow in the midplane of the channel, coming from the side to minimize reflection. The particle images are recorded using a 12-bit digital PCO SensiCam camera with a full-frame resolution of 1280×1024 px^2. For each of the four measured configurations, five series of 1000 PIV images were recorded to sample all parts of the channel, as indicated in Fig. 2. The images are processed with the cross-correlation PIV algorithm called WIDIM, based on an iterative multigrid predictor-corrector approach [42]. The image quality is optimized with the use of a background substractor that removes a combination of the mean and rms intensity levels from each pixel of the recorded fields.

A hot wire is also used to acquire the mean velocity and turbulence profiles along the porous plate to check the uniformity of the injection and to set the velocity inlet condition in the numerical simulations.

Numerical Simulations

The Taylor model is a powerful theoretical description of the flow to compare with PIV measurements when analyzing the mean velocity field. But this theory does not take into account the turbulent behavior of the real flow, measured by PIV. Therefore, unsteady numerical simulations are performed for three different configurations (Table 1) using the incompressible LES module of the commercial solver Fluent. The computational domain respects the size of the experimental model, except that its width is 1 mm (3-D domain for LES).

The meshes are composed of hexahedral cells, with refinements near the injection wall and the upper wall. The total number of cells ranges from 60,000 to 180,000, depending on the channel height. The topology of the grid, including the number of mesh points, is based on the work of Lupoglazoff and Vuillot [43], who performed a grid convergence study for a similar geometry than our configuration 1 (same length of the domain but different height: 20 mm rather than 23 mm). They showed that coherent structures are not observed when using only 20,000 cells, and that a minimum mesh size of 80,000 is necessary to capture the smaller structures of vortex

shedding. In the present investigation, after taking into account the height difference, the mesh size of Lupoglazoff and Vuillot is still increased by around 30% as a safety factor, which leads to a numerical domain of 120,000 grid cells for configuration 1.

The upper- and head-end boundaries are set as wall and the lower plane is set as velocity inlet. The outflow boundary condition in Fluent is used at the rear-end plane, which allows not to define any conditions at that outlet plane because Fluent extrapolates the required information from the interior. Because there is no constant pressure imposed at the outlet condition, the generation of spurious acoustic waves when vortices are leaving the domain is then limited. Anyway, the incompressible solver does not account for acoustic wave propagation within the domain. Periodic condition is defined at the two lateral surfaces to simulate a channel of infinite width, which leads to a two-dimensional behavior. A constant normal velocity is imposed along the velocity inlet boundary. The inlet turbulence quantities are chosen to be uniform, the turbulence intensity (TI) level and the hydraulic diameter being calculated from the experimental setup dimensions. For the LES model, the vortex method is chosen: the perturbation is added on the mean velocity via a fluctuating vorticity field.

For each configuration, a Reynolds-averaged Navier–Stokes simulation using the RNG k-ϵ model with enhanced wall treatment is performed to act as an initial condition. Then the LES is done, using the Smagorinsky model. The timestep is initially chosen to satisfy the condition CFL < 1, based on the minimum cell size and the maximum velocity (calculated from the Taylor theoretical flow). Then, the timestep is adapted to fasten the simulation, keeping the Courant–Friedrichs–Lewy (CFL) always smaller than 0.4. The total LES computational time equals 15 flow throughs (FTs), the time required for a particle to travel the numerical domain. As shown by Tóth [44], three FTs are necessary to get rid of the transient part and reach the typical flow pattern. This is also confirmed when observing in Fig. 3a the instantaneous vorticity field obtained after three FTs. From all the instantaneous flowfields taken from the 12 remaining FTs, the first- and second-order statistical moments of the velocity (mean and rms) are determined.

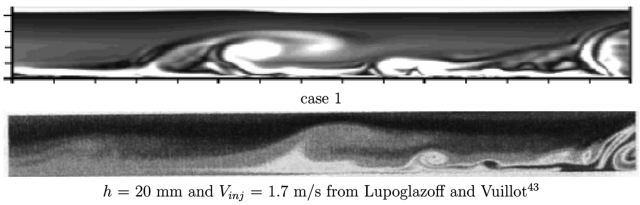

Fig. 3 Comparison of the results with the one obtained by Lupoglazoff [33].

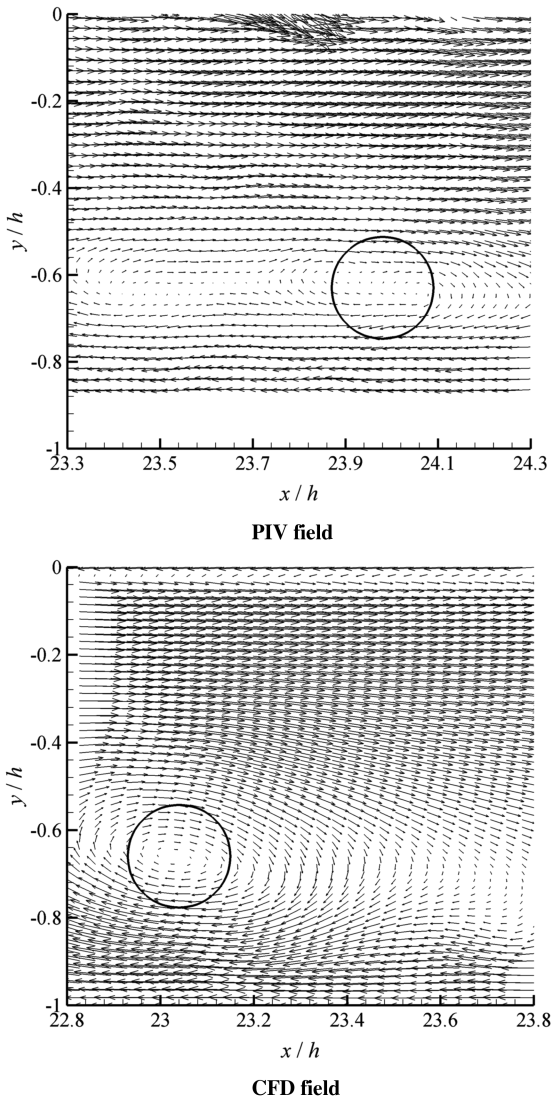

Fig. 4 Sample of a detected vortex in a PIV and CFD instantaneous field.

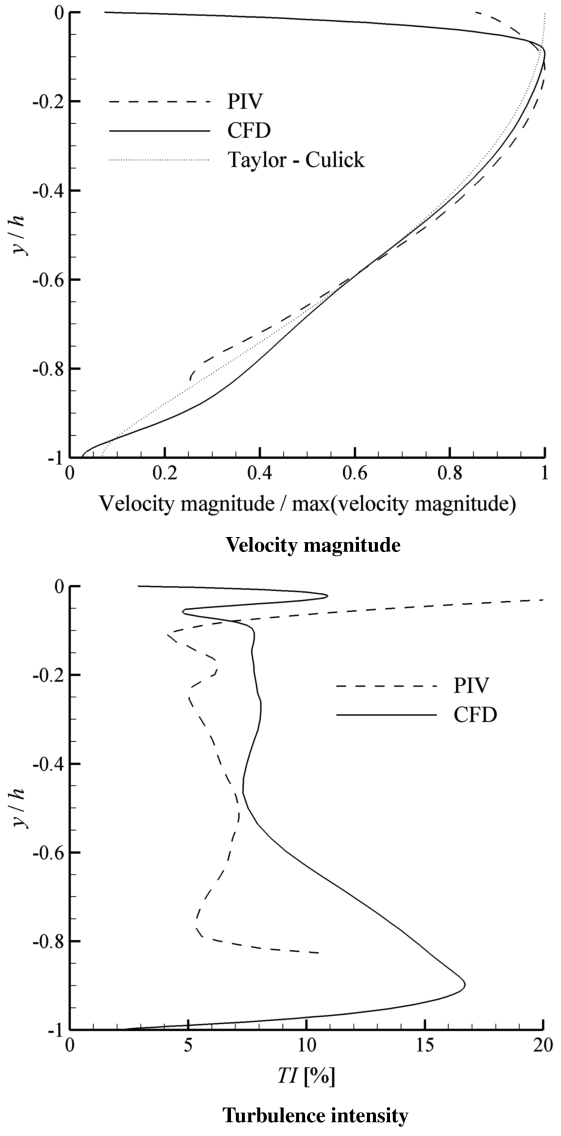

Fig. 5 Transversal profiles of the nondimensional velocity magnitude and TI at $x = 530$ mm.

As a first validation of the results, Fig. 3 compares one vorticity field of the nominal configuration and the entropy field obtained by Lupoglazoff and Vuillot [43] for an injection velocity of $V_{\text{inj}} = 1.7$ m/s and a channel height of $h = 20$ mm. Qualitatively, the two fields are matching very well as similar vortical structures are appearing in the domain.

Validation of Computational Fluid Dynamics Data

The validation of the computational fluid dynamics (CFD) data is based on the nominal configuration (case 1 in Table 1). The comparison is focusing on the mean velocity profiles, the TI profiles, and the statistical characteristics of the vortices detected by VKI wavelet software. Figure 4 provides two instantaneous fields, from both PIV and CFD, where a vortex is identified. The velocity magnitude at the core of the vortex is subtracted from the velocity field. As shown in the figure, there is good agreement in the transversal position and in the size of the vortex. These observations will be validated later in this paper thanks to a statistical analysis of the detected vortices.

Figure 5 gives transversal profiles of the mean velocity magnitude and TI to compare the PIV and CFD results at one given position with the theoretical Taylor–Culick flow (only for the mean velocity) defined as

$$\begin{cases} U = \frac{\pi}{2} x \cos(\frac{\pi y}{2}) \\ V = -\sin(\frac{\pi y}{2}) \\ W = 0 \end{cases}$$

The presented velocity profiles are normalized by dividing the y position by the channel height h and the velocity magnitude by its maximum value. A good agreement is observed between the different curves for the mean velocity. Because of remaining reflections, PIV data are not correct close to the walls. The TI is defined as the ratio between the rms velocity magnitude and the maximum value of the velocity profile. Figure 5b shows that the orders of magnitude are fitting quite well between the numerical and experimental data, but the shape of the profiles are not really similar.

Based on the mean flow, it is difficult to conclude correctly on the presence of coherent structures and on their influence. Therefore, a statistical analysis of the detected vortices in the different fields is performed using Wave2006, a software developed at VKI by Schram et al. [45]. This software is first computing the λ field, which is the nonzero eigenvalue of $S^2 + \Omega^2$ (S and Ω are, respectively, the symmetric and antisymmetric part of the velocity gradient tensor). Taking only the negative part of this quantity, the swirling motion of the flow can be distinguished from the shear motion. Then the vortices are detected with the wavelet transform applied to the λ field, using the 2-D Marr function (Mexican hat) as mother wavelet. From all the detected vortices, a statistical analysis of their properties (such as the diameter, the vertical position, etc.) is performed. Only the vortices with a diameter bigger than 3 mm ($D/h = 0.13$) are taken into account, following a commonly used rule that a detected vortex has to be composed of at least five vectors across its diameter [44] (in this case approximately 3 mm).

Figure 6 represents the statistical properties of the detected vortices for the numerical and experimental results. The number of vortices is normalized by the total number of analyzed images, because this number is not the same for CFD (344) and PIV (999).

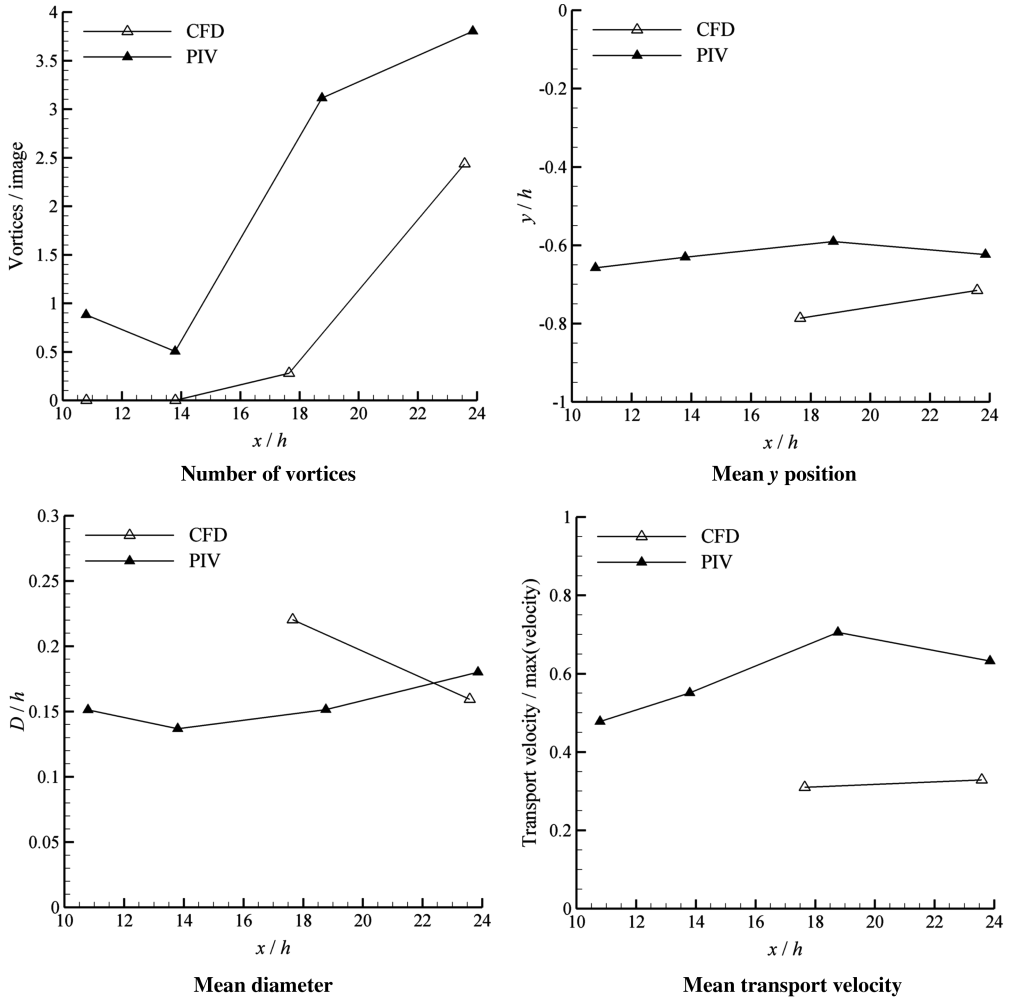

Fig. 6 Statistical properties of the detected vortices for PIV and CFD.

The number of vortices per field is similar for PIV and CFD, which suggests that the main phenomenon is correctly resolved by CFD. Also, the slope of the two lines is approximately the same, but they are shifted; the growing of the vortices is appearing almost in the middle of the channel for the PIV and in the last third of the channel for the CFD. This is probably due to the higher turbulence near the injection plane in the experimental setup (porous plate, injection of oil, etc.) that forces the creation of the vortices quicker than what is observed in the CFD. Figure 6b represents the mean y position for the numerical and experimental results, and this mean position is similar for the two cases. Figure 6c shows the mean diameter of the vortices, normalized by the channel height. The diameter of the PIV vortices is increasing while the one from CFD is decreasing, getting closer to the PIV results at the end of the channel. Finally, Fig. 6d shows the transport velocity of the vortices normalized by the maximum velocity magnitude at the position of the analysis. The vortices detected in the PIV field have a higher transport velocity compared with the ones of the CFD. This is due to their position in the channel height, which is further from the injection wall for the PIV case.

From the previous analysis, it can be concluded that the numerical simulations have been validated and that the two approaches can be used to determine the influence of the parameters: the injection velocity and the channel height.

Influence of the Injection Velocity

The influence of the injection velocity is analyzed through the PIV data, because for each of the two channel heights (23 mm and 33 mm) two configurations are available where only the injection velocity is changing, while for the CFD data both the injection velocity and the channel height are varying between the configurations. Two injection velocities are considered: 1 m/s and 1.5 m/s. The mean flow is investigated for the 33 mm channel height test case, and the vortical content is analyzed using the 23 mm test case because it has been proven in the previous section that coherent structures are present in the flow.

Figure 7a represents the transversal profile of the nondimensional velocity magnitude at $x = 530$ mm for the 33 mm channel height test case. The deviation from the Taylor model is larger when the injection velocity is lower. Figure 7b shows the evolution of the TI for two different axial positions. The TI is much higher in the first axial position. The influence of the upstream wall can be a cause. Another reason is the blockage of the porous plate by oil, which always starts at the extremities of the plate (the beginning and ending of the channel) and which could induce more inlet turbulence. Increasing the injection velocity augments the TI amplitude, but the shape of the profiles is not changed from one velocity to another.

Figure 8a represents the number of detected vortices per image for a channel height of 23 mm because it has been proven in the previous section that coherent structures are present in the flow for that channel height. The evolution of this quantity is highly dependent on the velocity. For the lower injection velocity, the number of vortices increases until the middle of the channel and then decreases. At the same time, the mean diameter of the vortices remains approximately constant (the range of diameter in Fig. 8b is only 1.2 mm, corresponding to a range of D/h of 0.05). However, only the vortices with diameter bigger than 3 mm are taken into account for this analysis. It means that the vortices formed in the first half of the channel are split into smaller ones (smaller than 3 mm), when moving to the end of the channel. Looking to the higher injection velocity, the number of vortices is increasing with a relatively high rate in the second half of the channel so that the splitting of vortices observed previously seems to disappear when the velocity is increasing. The influence of the injection velocity on the statistical properties (y position, diameter, transport velocity) is quite small. As an example, Fig. 8b shows the mean diameter where there is no clear distinction between the two injection velocities.

From all these results, the modifications between the two injection velocities are quite small, which tends to conclude that the injection velocity plays a minimal role in the determination of the flow behavior. The only small difference is observed on the number of vortices detected by the wavelet analysis, the other properties of the vortices being independent of the injection velocity.

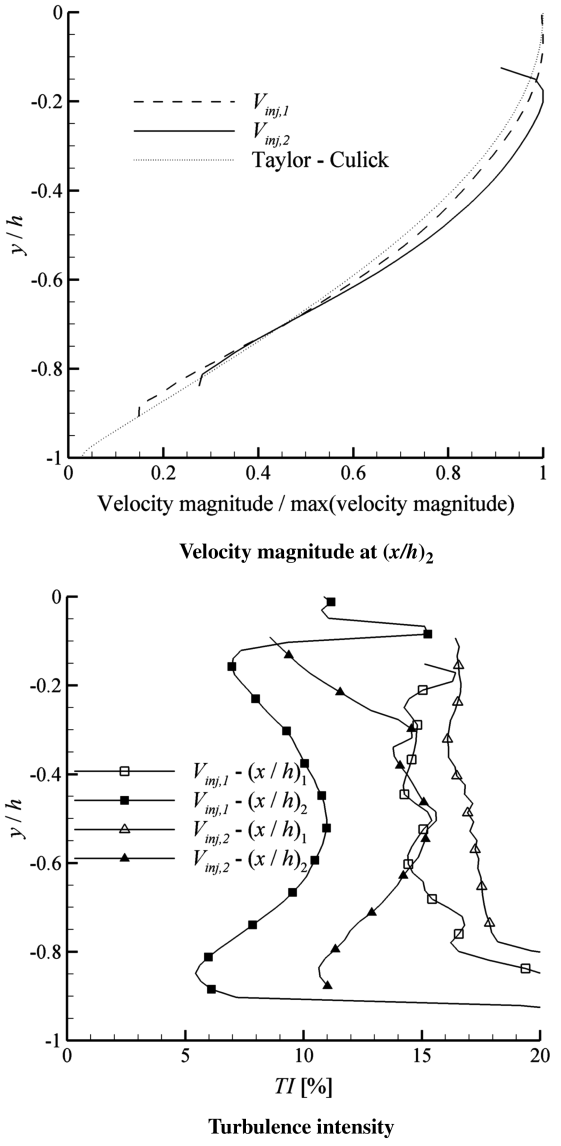

Fig. 7 Influence of the injection velocity on the mean flow. Transversal profiles for $h = 33$ mm. $V_{\mathrm{inj},1} = 1$ m/s, $V_{\mathrm{inj},2} = 1.5$ m/s, $(x/h)_1 = 6.7$, $(x/h)_2 = 16.1$.

Influence of the Channel Height

This analysis is performed based on the CFD results (cases 1, 3, and 5), because only two channel heights were tested with PIV. Although the CFD configurations are considering different injection velocities, it has been proven previously that this influence on the flow development is quite small. Three channel heights are considered: 13, 23, and 33 mm.

Figure 9c shows an instantaneous vorticity field for the nominal configuration ($h = 23$ mm). Looking at this contour, a huge vorticity zone emerges from the injection plane and rolls up to form a vortical structure. At the end of the channel, this structure meets small vortices coming from the injection plane and merges into a big vortical structure with some smaller vortices inside. For $h = 13$ mm (the channel is split in three parts and only the last two thirds are shown in Figs. 9a and 9b), the coherent structures appear at the second third of the channel (instead of the third one for the nominal configuration), and the roll up of vorticity zones is present and more dense than in the nominal configuration (Fig. 9c). In the last third of the channel, these structures take some vortices created near the injection plane to form a big cluster containing a lot of smaller

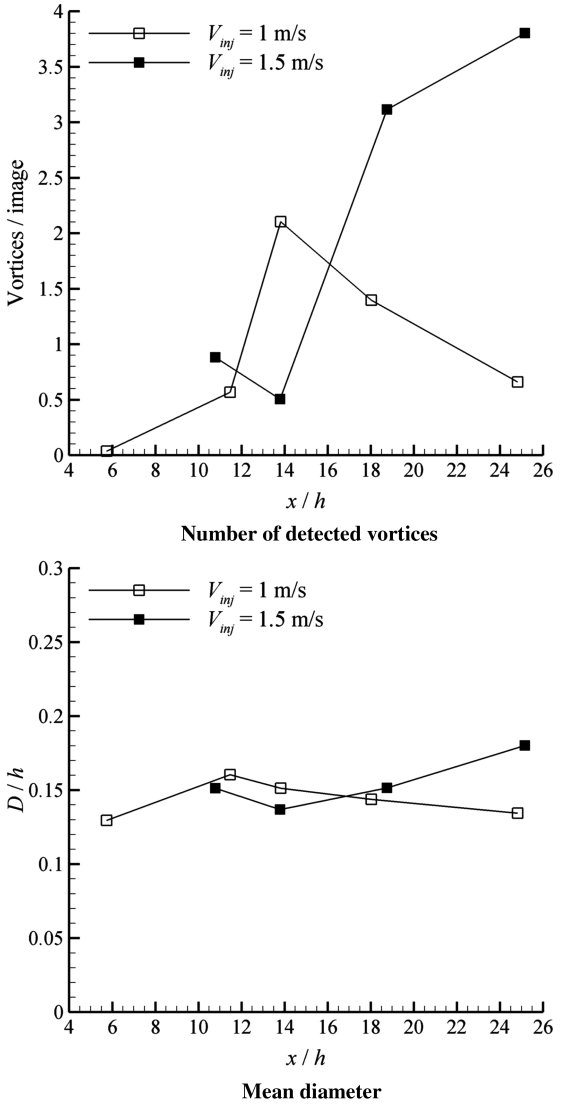

Fig. 8 Influence of the injection velocity on statistical properties of the coherent structures for $h = 23$ mm.

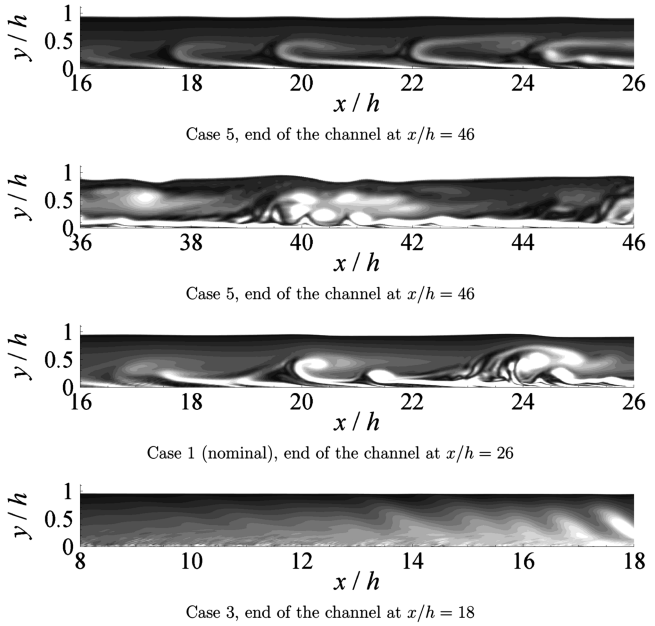

Fig. 9 Influence of the channel height: case 5 ($h = 13$ mm), case 1 ($h = 23$ mm), and case 3 ($h = 33$ mm).

vortices inside. For $h = 33$ mm, there is no vortical structure in the channel. A small roll up of the vorticity appears when starting the LES computation, but it is only the consequence of the initial perturbation and the flow is not able to sustain it, as indicated by Fig. 9d.

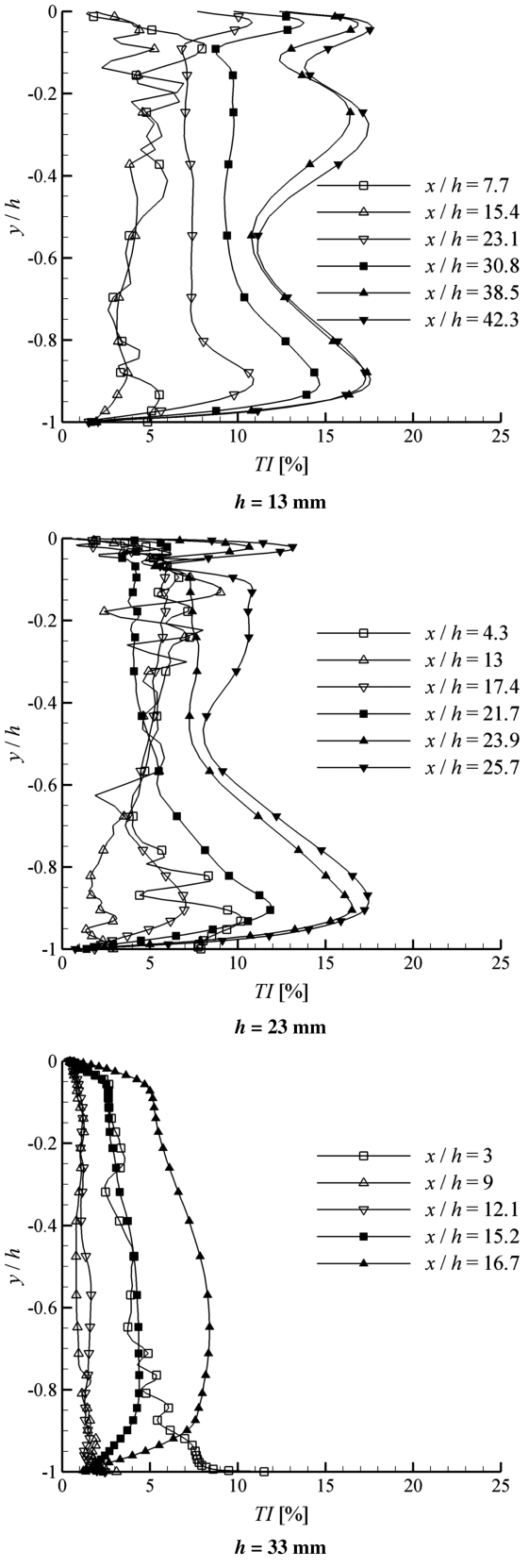

Fig. 10 Evolution of the TI with the axial position for three different channel heights.

Table 2 Comparison of the values of x_S and x_D given by Griffond [46] and the CFD results

	h [mm]		x_S (-)		x_D (-)	
	Griffond	VKI	Griffond	VKI	Griffond	VKI
5	10	13	60	46	——	15.4
1	20	23	30	26	18.7	17.4
3	30	33	20	18	∼20	——

All these results are in agreement with a theoretical analysis proposed by Griffond [46]. This theory is defining two nondimensional axial positions: x_S is the channel outlet position and x_D is the position where the coherent structures are produced. Table 2 gives the values of these axial positions, both from the thesis of Griffond (from experiments performed using the VECLA setup) and from our numerical simulations. Based on these three positions, the third case has $x_S < x_D$, and so there is no coherent structures appearing. For the two other cases $x_D < x_S$ and, therefore, structures are produced. Looking to the CFD results, the values deduced from the vorticity contours are smaller than the experiments. That difference is difficult to explain because a lot of parameters could influence this determination (validity of the theory, precision of VECLA measurements, difference of conditions between experiments and the CFD, precision of the CFD, etc.).

The analysis of the vorticity fields allows us to understand the influence of the channel height on the development of the turbulent structures in the flow. An analysis of the turbulent intensity profiles will link the previous visualization to a better understanding of the differences in the flow behavior. The transversal TI profiles are provided in Fig. 10 for the three channel heights and for different axial positions. The definition of the TI is the same as in the previous sections. Looking first at the smallest channel height ($h = 13$ mm), the TI profiles are almost flat in the first third of the channel, reflecting the laminar behavior of the flow (Fig. 10a). Then, a bump in the profile appears in the second third of the channel, reflecting the transition to turbulence and the appearance of structures. The turbulence then develops gradually when moving toward the outlet until reaching an almost constant value in the last third of the channel. As the major part of the flow with a channel height of 13 mm is turbulent, and the laminar part is really short, it can therefore be considered that the flow for this channel height has a turbulent behavior. Looking now to the nominal configuration ($h = 23$ mm, Fig. 10b), a laminar behavior is observed up to the end of the second third of the channel. In the last third the typical bump shape appears, reflecting a transitional behavior, and the turbulent behavior of the flow is observed only at the very end of the channel. Therefore, the flow for this channel height is referred as transitional. Finally, the last configuration ($h = 33$ mm, Fig. 10c) is presenting flat TI profiles with low values in almost all the channel length. At the very end of the channel, the TI is increasing significantly. But the bump observed in the previous configuration is not visible here, which is coherent with the vorticity field where no structures are observed. It can therefore be concluded that the flow behavior for a channel height of 33 mm is laminar.

Conclusions

The objectives of this study were multiple. The first one was the measurement of velocity fields using PIV in a channel where the flow is injected through a porous plate. This objective was achieved by improving the injection system and using a special laser sheet to illuminate the channel. The processing of the acquired images was also important because it allowed to increase the image quality especially near the upper wall and the injection plane.

The second objective was to perform PIV measurements in different configurations of the experimental setup, which allowed the generation of an experimental database. Four configurations of five fields were tested, using two injection velocities and two channel heights. These measurements were analyzed in two ways, first using the mean velocity magnitude and the TI computed, thanks to a statistical analysis of the 1000 images of each field, and secondly using the wavelet software developed at VKI to get statistical information about the characteristics of the vortices present in the flow. From the analysis of these results, it can be concluded that a transitional behavior is observed for a channel height of 23 mm, and the injection velocity showed a minor influence of the flow behavior.

In addition, numerical simulations were performed in complement to the PIV results. Three cases were computed to investigate the different types of flow regime: laminar, transitional, and turbulent. The configuration with a channel height of 23 mm is matching quite well with the experiments. The simulations were an important tool to understand how the structures are emerging from the injection plane, and how they are modified when traveling to the channel exit. From the three cases, three different behaviors can be observed. The configuration with $h = 33$ mm is showing a laminar behavior, without any vortices, flat TI profiles, etc. The configuration with $h = 23$ mm shows a transitional behavior, with an almost laminar part in the beginning of the channel, and the development of coherent structures dissipating into big clusters of smaller vortices. And for the last case $h = 13$ mm, the development of the coherent structures is almost similar to the previous case, but it appears in a very upstream position. Even the beginning of the channel is showing some vorticity zones, which means that this flow is almost turbulent everywhere. All these cases are showing an abscissa of generation of the structures in agreement with the theory of Griffond.

References

[1] Taylor, G., "Fluid Flow in Regions Bounded by Porous Surfaces," *Proceedings of the Royal Society of London, Series A: Mathematical and Physical Sciences*, Vol. 234, No. 1199, 1956, pp. 456–475. doi:10.1098/rspa.1956.0050

[2] Culick, F., "Rotational Axisymmetric Mean Flow and Damping of Acoustic Waves in a Solid Propellant Rocket," *AIAA Journal*, Vol. 4, No. 8, 1966, pp. 1462–1464. doi:10.2514/3.3709

[3] Dotson, K., Koshigoe, S., and Pace, K., "Vortex Shedding in a Large Solid Rocket Motor Without Inhibitors at the Segment Interfaces," *Journal of Propulsion and Power*, Vol. 13, No. 2, 1997, pp. 197–206. doi:10.2514/2.5170

[4] Mason, D. R., Folkman, S. L., and Behring, M., "Thrust Oscillations of the Space Shuttle Solid Rocket Booster Motor During Static Tests," AIAA Paper 79-1138, 1979.

[5] Blomshield, F. S., and Mathes, H. B., "Pressure Oscillations in Post-Challenger Space Shuttle Redesigned Solid Rocket Motors," *Journal of Propulsion and Power*, Vol. 9, No. 2, 1993, pp. 217–221. doi:10.2514/3.23612

[6] Brown, R. S., Dunlap, R., Young, S. W., and Waugh, R. C., "Vortex Shedding as a Source of Acoustic Energy in Segmented Solid Rockets," *Journal of Spacecraft and Rockets*, Vol. 18, No. 4, 1981, pp. 312–319. doi:10.2514/3.57822

[7] Scippa, S., Pascal, P., and Zanier, F., "Ariane-5 MPS: Chamber Pressure Oscillations Full Scale Firings Results Analysis and Further Studies," AIAA Paper 94-3068, 1994.

[8] Prévost, M., Vuillot, F., and Traineau, J. C., "Vortex Shedding Driven Oscillations in a Subscale Motor for the Ariane 5 MPS Solid Rocket Motors," AIAA Paper 96-3247, 1996.

[9] Traineau, J. C., Prévost, M., Vuillot, F., Le Breton, P., Cuny, J., Preioni, N., and Bec, R., "Subscale Test Program to Assess the Vortex Shedding Driven Instabilities in Segmented Solid Rocket Motors," AIAA Paper 97-3247, 1997.

[10] Vuillot, F., "Vortex-Shedding Phenomena in Solid Rocket Motors," *Journal of Propulsion and Power*, Vol. 11, No. 4, 1995, pp. 626–639. doi:10.2514/3.23888

[11] Mombelli, C., Guichard, A., Godfroy, F., and Guéry, J.-F., "Parallel Computation of Vortex Shedding in Solid Rocket Motors," AIAA Paper 99-2510, 1999.

[12] Anthoine, J., Buchlin, J.-M., and Guéry, J.-F., "Effect of Nozzle Cavity on Resonance in Large SRM: Numerical Simulations," *Journal of Propulsion and Power*, Vol. 19, No. 3, 2003, pp. 374–384. doi:10.2514/2.6141

[13] Cosyn, P., Vierendeels, J., and Anthoine, J., "Numerical Simulation of Aeroacoustic Phenomena in a Solid Rocket Booster," *Journal of Spacecraft and Rockets*, Vol. 42, No. 1, 2005, pp. 111–117. doi:10.2514/1.3579

[14] Culick, F. E. C., and Magiawala, K., "Excitation of Acoustic Modes in a Chamber by Vortex Shedding," *Journal of Sound and Vibration*, Vol. 64, No. 3, 1979, pp. 455–457. doi:10.1016/0022-460X(79)90591-1

[15] Dunlap, R., and Brown, R. S., "Exploratory Experiments on Acoustic Oscillation Driven by Periodic Vortex Shedding," *AIAA Journal*, Vol. 19, No. 3, 1981, pp. 408–409. doi:10.2514/3.7783

[16] Mettenleiter, M., Haile, E., and Candel, S., "Adaptive Control of Aeroacoustic Instabilities," *Journal of Sound and Vibration*, Vol. 230, No. 4, 2000, pp. 761–789. doi: 10.1006/jsvi.1999.2659.

[17] Anthoine, J., Buchlin, J.-M., and Hirschberg, A., "Effect of Nozzle Cavity on Resonance in Large SRM: Theoretical Modeling," *Journal of Propulsion and Power*, Vol. 18, No. 2, 2002, pp. 304–311. doi:10.2514/2.5935

[18] Guéry, J.-F., Avalon, G., Vuillot, F., Plourde, F., Anthoine, J., and Platet, B., "Use of Cold Flow Experiments in the ASSM Program: Lessons and Results," *2nd European Conference on Launcher Technology*, European Space Agency, Noordwijk, The Netherlands, Nov. 2000.

[19] Vetel, J., Plourde, F., Doan-Kim, S., and Prévost, M., "Cold Gas Simulation of the Influence of Inhibitor Shape in Combustor Combustion," *Journal of Propulsion and Power*, Vol. 21, No. 6, 2005, pp. 1098–1106. doi:10.2514/1.7445

[20] Nguyen, C., Plourde, F., and Doan-Kim, S., "Analysis of Injecting Wall Inclination on Segmented Solid Rocket Motor Instability," *Journal of Propulsion and Power*, Vol. 24, No. 2, 2008, pp. 213–223. doi:10.2514/1.29551

[21] Anthoine, J., and Lema, M., "Passive Control of Pressure Oscillations in Solid Rocket Motors: Cold-Flow Experiments," *Journal of Propulsion and Power*, Vol. 25, No. 3, 2009, pp. 792–800. doi:10.2514/1.39794

[22] Vuillot, F., "Vortex-Shedding Phenomena in Solid Rocket Motors," *Journal of Propulsion and Power*, Vol. 11, No. 4, 1995, pp. 626–639. doi:10.2514/3.23888

[23] Kourta, A., "Shear Layer Instability and Acoustic Interaction in Solid Propellant Rocket Motors," *International Journal of Numerical Fluid Mechanics*, Vol. 25, 1997, pp. 973–981. doi:10.1002/(SICI)1097-0363

[24] Mombelli, C., Guichard, A., Godfroy, F., and Guéry, J.-F., "Parallel Computation of Vortex Shedding in Solid Rocket Motors," *Proceedings of the 35th AIAA/ASME/SAE/ASEE Joint Propulsion Conference and Exhibit*, AIAA Paper 99-2510, 1999.

[25] Hulshoff, S. J., Hirschberg, A., and Hofmans, G. C. J., "Sound Production of Vortex Nozzle Interaction," *Journal of Fluid Mechanics*, Vol. 439, 2001, pp. 335–352. doi:10.1017/S0022112001004554

[26] Apte, A., and Yang, V., "Unsteady Flow Evolution in Porous Chamber with Surface Mass Injection, Part 1: Free Oscillation," *AIAA Journal*, Vol. 39, No. 8, 2001, pp. 1577–1586. doi:10.2514/2.1483

[27] Apte, A., and Yang, V., "Unsteady Flow Evolution in Porous Chamber with Surface Mass Injection, Part 2: Acoustic Excitation," *AIAA Journal*, Vol. 40, No. 2, 2002, pp. 244–253. doi:10.2514/2.1666

[28] Apte, A., and Yang, V., "Large-Eddy Simulation Study of Transition and Flow Instability in a Porous-Walled Chamber with Mass Injection," *Journal of Fluid Mechanics*, Vol. 477, March 2003, pp. 215–225. doi:10.1017/S0022112002002987

[29] Vetel, J., Plourde, F., Doan-Kim, S., and Guéry, J.-F., "Numerical Simulations of Wall and Shear-Layer Instabilities in Cold Flow Setup," *Journal of Propulsion and Power*, Vol. 19, No. 2, 2003, pp. 297–306. doi:10.2514/2.6111

[30] Plourde, F., Najjar, F., Vetel, J., Wasistho, B., Doan-Kim, S., and Balachandar, S., "Numerical Simulations of Wall and Shear-Layer Instabilities in a Cold Flow Setup," AIAA Paper 2003-4674, July 2003.

[31] Flandro, G., "Vortex Driving Mechanism in Oscillatory Rocket Flows," *Journal of Propulsion and Power*, Vol. 2, No. 3, 1986. doi:10.2514/3.22871

[32] Brown, R., Dunlap, R., Young, S., and Waugh, R., "Vortex Shedding as a Source of Acoustic Energy in Segmented Solid Rockets," *Journal of Spacecraft and Rockets*, Vol. 18, No. 4, 1981. doi:10.2514/3.57822

[33] Lupoglazoff, N. and Vuillot, F., "Parietal Vortices Shedding as a Cause of Instability for Long Solid Propellant Motors. Numerical Simulations and Comparisons with Firing Tests," AIAA Paper 96-0761, 1996.

[34] Flandro, G. A., and Majdalani, J., "Aeroacoustic Instability in Rockets," *AIAA Journal*, Vol. 41, No. 3, 2003, pp. 485–497. doi:10.2514/2.1971

[35] Chedevergne, F., Casalis, G., and Feraille, T., "Biglobal Linear Stability Analysis of the Flow Induced by Wall Injection," *Physics of Fluids*, Vol. 18, No. 1, 2006. doi:10.1063/1.2160524

[36] Raffel, M., Willert, C., and Kompenhans, J., *Particle Image Velocimetry: A Practical Guide*, Springer, New York, 1998.

[37] Anthoine, J., Mettenleiter, M., Repellin, O., Buchlin, J.-M., and Candel, S., "Influence of Adaptive Control on Vortex Driven Instabilities in a Scaled Model of Solid Propellant Motors," *Journal of Sound and Vibration*, Vol. 262, No. 5, May 2003, pp. 1009–1046. doi:10.1016/S0022-460X(02)01034-9

[38] Anthoine, J., "Experimental and Numerical Study of Aeroacoustic Phenomena in Large Solid Propellant Boosters," Ph.D. Thesis, Université Libre de Bruxelles, 2000.

[39] Avalon, G., and Lambert, D., "Montage Valdo, Premiers Essais de Mise au Point et de Qualification," ONERA, Rept. 5/00064 defa, ONERA, 2000.

[40] Avalon, G., and Lambert, D., "Caractérisation des Phénomènes Liés L'instabilité Naturelle de L'écoulement dans le Montage VECLA, Etude des Conditions Permettant de Réaliser L'accrochage Acoustique," ONERA, Rept. CNES 90/6133 EY, 1997.

[41] Couton, D., Plourde, F., Vetel, J., and Doan Kim, S., "Le Couplage Aéro-Acoustique et sa Caractérisation sur un Montage en Gaz Froid: MICAT1," *Ecoulements Internes en Combustion Solide*, Vol. 3, CNES/ONERA, Poitier, France, 1998, pp. 211–218.

[42] Riethmuller, M., and Scarano, F., "Iterative Multigrid Approach in PIV Image Processing with Discrete Window Offset," *Experiments in Fluids*, Vol. 26, No. 6, 1999, pp. 513–523. doi:10.1007/s003480050318

[43] Lupoglazoff, N., and Vuillot, F., "Numerical Simulations of Parietal Vortex-Shedding Phenomenon," *34th AIAA/ASME/SAE/ASEE Joint Propulsion Conference and Exhibit*, AIAA, Reston, VA, 1998, p. 108.

[44] Tóth, B., "Two-Phase Flow Investigation in a Cold-Gas Solid Rocket Motor Model Through the Study of the Slag Accumulation Process," Ph.D. Thesis, Université Libre de Bruxelles, 2008.

[45] Schram, C., Rambaud, P., and Riethmuller, M., "Wavelet Based Structure Eduction from a Backward Facing Step Flow Investigated Using Particle Image Velocimetry," *Experiments in Fluids*, Vol. 36, No. 2, 2004, pp. 233–245. doi:10.1007/s00348-003-0695-9

[46] Griffond, J., "Instabilité Pariétale et Accrochage Aéroacoustique dans les Conduits à Parois Débitantes Simulant les Moteurs Propergol Solide D'Ariane 5," Ph.D. Thesis, Ecole Nationale Supérieure de l'Aéronautique et de l'Espace, 2001.

R. Rangel
Associate Editor